LETTER

Enhanced mechanical properties of Q-carbon nanocomposites by nanosecond pulsed laser annealing

To cite this article: Siddharth Gupta *et al* 2018 *Nanotechnology* **29** 45LT02

Enhanced mechanical properties of Q-carbon nanocomposites by nanosecond pulsed laser annealing

Siddharth Gupta [1], Ritesh Sachan [1, 2], Anagh Bhaumik [1], Jagdish Narayan [1, *]

[1] Department of Materials Science and Engineering, Centennial Campus
North Carolina State University, Raleigh, NC 27695-7907, USA

[2] Materials Science Division, Army Research Office, Research Triangle Park, NC 27709, USA

*Corresponding Author E-mail: narayan@ncsu.edu (Jagdish Narayan)

Abstract

Q-carbon is a metastable phase of carbon formed by melting and subsequently quenching amorphous carbon films by nanosecond laser in a super undercooled state. As Q-carbon is a material harder than diamond, it makes an excellent reinforcing component inside the softer matrix of a composite coating. In this report, we present a single-step strategy to fabricate adherent coatings of hard and lubricating Q-carbon nanocomposites. These nanocomposites consist of densely-packed sp^3-rich Q-carbon (82% sp^3), and sp^2-rich (40% sp^3) α-carbon amorphous phases. Nanoindentation tests showed that the Q-carbon nanocomposites exhibit a hardness of 67 GPa (Young's modulus ~840 GPa) in contrast to the soft α-carbon (hardness ~18 GPa). The high hardness of Q-carbon nanocomposites results in 0.16 energy dispersion coefficient, in comparison with 0.74 for α-carbon. The soft α-carbon phase provides lubrication, resulting in low friction and wear coefficients of 0.09 and $1x10^{-6}$, respectively, against the diamond tip. The nanoscale dispersion of hard Q-carbon and soft α-carbon phases in the Q-carbon nanocomposites enhances the toughness of the coatings. We present detailed structure-property correlations to understand enhancement in the mechanical properties of Q-carbon nanocomposites. This work provides insights into the characteristics of Q-carbon nanocomposites and advances carbon-based superhard materials for longer lasting protective coatings and related applications.

1. Introduction

Protective coatings for tribological applications have three essential requirements – hardness, toughness, and adhesion with the underlying substrate. Diamond and diamond-like carbon (DLC) protective coatings have played a significant role in advancing the materials systems by virtue of their high hardness, low coefficient of friction, inert behavior, and biocompatibility. Diamond coatings have high hardness but often exhibit short life-span due to poor adhesion, particularly on ferrous substrates comprising 3*d* transition metals due to the interposing weak graphitic layers. The mechanism of weak graphitic interposing layer formation on 3*d* transition metals has been discussed previously. These coatings also have lower toughness due to lack of dislocation generation during crack propagation. [1]

Unlike diamond, DLC thin films have an amorphous structure with a mixture of sp^3 and sp^2 bonded carbon and reduced hardness. Compressive stresses are one of the essential requirements for the formation of highly tetrahedral (sp^3) bonding. [2] The hardness of DLC coatings increases with sp^3 content, which simultaneously gives rise to compressive stresses, deteriorating the film/substrate adhesion. While it is possible to fabricate DLC films with high hardness (50-70 GPa), they have high intrinsic compressive stress, which in turn limits the thickness of the coating, because of adhesion failure. [3] Additives like Cr [4], Ta [5] and Nb [6] have been incorporated to improve the mechanical properties of DLC coatings by alleviating the compressive stress, at the cost of reduced hardness. Above 350^{o}C, DLC coatings are thermally unstable and undergo significant graphitization and oxidation.[7] Due to their industrial importance, many scientific studies have concentrated on DLC and diamond coatings to improve adhesion, wear resistance, thermal stability and toughness. The challenge in improving the performance of protective coatings for tribological applications is to fabricate hard and tough coatings, which exhibit significant wear resistance low friction coefficient and improved adhesion with the substrate for extended wear cycles. To address the difficulty in obtaining these properties in a single coating, we have designed novel nanocomposite coatings to improve the toughness, hardness of coatings and adhesion with the substrate simultaneously.

Pulsed laser annealing (PLA) is the most efficient and widely used method for introducing compressive stresses and enhancing the fatigue performance of metals.[8] Post-PLA, the heat flow is spatially and temporally confined, making it an ideal technique to melt materials like carbon, which are susceptible to sublimation. The first successful experiment pertaining to conversion of carbon in graphitic phase to pristine diamond was demonstrated by Narayan et al. by irradiating carbon implanted copper with nanosecond laser pulses. [9] This paper is based on our recent discovery of Q-carbon and direct conversion of amorphous carbon into diamond[10], at ambient temperature and pressure. By controlling the extent of undercooling, the metallic carbon melt can be quenched directly into graphite, diamond or Q-carbon.[11] The Q-carbon quenched from the liquid is a new state of solid carbon with a higher mass density than amorphous carbon and a mixture of mostly fourfold sp^3 (75%–85%) with the rest being threefold sp^2 bonded carbon (with distinct entropy). It is an amorphous phase of carbon with nanocrystallites of diamonds embedded in it. The Q-carbon has shown many extraordinary properties: *harder* than diamond [10],[12], room-temperature ferromagnetism[13], field-emission[14] and high-temperature superconductivity[15],[16] upon doping with Boron. Interestingly, hardness and superconductivity are directly linked to each other through the McMillan-Hopfield equation: $T_c \approx 0.2[\lambda < \omega^2 >= \sum_i \eta_i/M_i]^{0.5}$. Here, λ is the electron-phonon coupling constant related to ratio of the spring constants, ω is averaged phonon frequency, M is averaged atomic mass, and η is the McMillan-Hopfield parameter with units of spring constant and is related to strength of electronic response of electrons near the Fermi surface to atomic perturbations. Thus, densely packed sp^3 and sp^2 bonded carbon-based materials offer the best hope for advancement in BCS high-temperature superconducting transition temperature (T_c) and superhard materials. The highest T_c in B-doped diamond obtained by CVD processing was reported to be 11 K, where B concentration is limited to the equilibrium atomic concentration of 2.0%. Since T_c was predicted to scale with B concentration in diamond, the field was at a standstill until the discovery of Q-carbon. By non-equilibrium laser melting and rapid quenching, we attained distinct concentrations of 17% and 25% at. of B in Q-carbon with a record T_c of 36[15] and 57 K[16], respectively. The Boron diffusion coefficient during the PLA of B-doped Q-carbon was calculated

to be ~2x10^{-8} m^2/s. Such a high diffusion coefficient corresponds to diffusion in the liquid state, providing the conclusive experimental evidence for melting of carbon by PLA processing. [15]

In this study, we have increased the quenching rate (10^{11} K s^{-1}) of the super-undercooled carbon melt state, to form Q-carbon nanocomposites. These nanocomposites consist of superhard Q-carbon nanostructures embedded in the α-carbon matrix. The amorphous α-carbon is formed when the as-deposited DLC is melted with very small undercooling and subsequently quenched. The hardness and mechanical characteristics of the material formed after melt regrowth have a strong dependence on the extent of undercooling. The contrast between composition and physical behavior of Q-carbon and α-carbon phases is characterized by Raman spectroscopy, scanning electron microscopy, atomic force microscopy, and hardness measurements. The friction and wear measurements highlight the significant improvement in mechanical properties of Q-carbon nanocomposites over DLC coatings. The dispersion of hard Q-carbon and soft α-carbon phases at nanoscale increases the toughness of composite films, showing a considerable improvement in durability of the nanocomposites against wear. We have also established that the increase in undercooling underpins the formation and resulting hardness and toughness characteristics of Q-carbon nanocomposites.

2. Experimental section

2.1 *Synthesis of Q-carbon nanocomposites*

DLC films are deposited on the r-sapphire substrates by laser ablation of glassy carbon target, using KrF excimer laser having 25 ns pulse duration, 248 nm wavelength, and energy density 3.5-4.0 J cm^{-2}, to a thickness of ~400 nm under the high vacuum of 1x10^{-6} Torr inside the pulsed laser deposition (PLD) chamber at room temperature. Subsequently, PLA was performed on DLC films, using a single pulse of ArF Excimer laser (193 nm; 20 ns) with 0.6-1.0 J cm^{-2} energy density at room temperature and pressure in air. The energy density was controlled using a converging lens, generating a spot size of 1.0 ± 0.01 cm^2.

2.2 *Characterization*

WITec confocal Raman microscope system (Alpha 300M) was utilized (532 nm source) to characterize the Raman-active vibrational modes in as-deposited and laser annealed samples. The Raman acquisitions were calibrated using single-crystal silicon with a characteristic Raman peak at 520.6 cm^{-1}. High-resolution scanning electron backscattering images were acquired for structural analysis, and phase identification was performed by FEI Verios 460L field-emission scanning electron microscope (FESEM). FEI Quanta 3D FEG scanning electron microscope (SEM) with the dual functionality of electron and FIB guns was used to fabricate the cross-sectional transmission electron microscopy (TEM) specimens, while keeping the protective platinum layer on, for accurate microstructural characterization and measurement of the C-C bonding characteristics. Low-energy and low-current gallium ions (5 kV; 10 pA) were utilized for final polishing to remove milling damage and roughness of the specimen, simultaneously. Gallium damage is particularly detrimental to the sp^3 nanoclusters, as it graphitizes the bombarded regions instantaneously. The FEI Titan 80-300 keV aberration-corrected scanning transmission electron microscope (STEM), operating at 200 keV, was utilized to perform high-angle-annular dark field (HAADF) imaging. The C-C bonding states of various polymorphs of carbon, i.e., diamond, as-deposited DLC and Q-carbon nanostructures were investigated by electron energy loss spectroscopy (EELS) with a resolution of 0.15 eV. The EELS data acquisition was carried out at 29 mrad collection angle. Both Raman spectroscopy and EEL spectroscopy were employed to analyze the sp^3/sp^2 bonding characteristics in all of the samples for internal consistency. Hysitron Ubi-1 Nanoindenter was utilized to perform *in-situ* scanning probe microscopy (SPM) and nanoindentation on as-deposited DLC, Q-carbon and α-carbon nanocomposite phases using a Berkovich diamond tip with a radius of curvature ~100 nm, to calculate hardness and Young's Modulus. Indents were made using an open loop system with symmetric 20 s loading-unloading and 10 s dwell time and 1 mN constant load. The measurements were calibrated at the same load, with fused Quartz and r-sapphire substrates as standard samples as shown in **Figure S1(a) and S1(b)**, respectively. Wear testing of

the specimens was performed using a conical diamond tip with 100 µm radius of curvature and 2 N reciprocating load, on NANOVEA triboindenter, utilizing a pin-on-disc arrangement.

3. Results and Discussion

3.1 Formation of Q-carbon nanocomposites

During PLD, plume energetics are used to control sp^3 content in the as-deposited DLC films. Point source plume generates ~30% sp^3, and forward directed plume increases sp^3 content to ~90%. The sp^3 fraction in the as-deposited DLC films was varied between 40-80%, which resulted in melting and successful Q-carbon formation upon PLA processing. After melting DLC, the liquid carbon undergoes super-undercooling at the substrate-melt interface, inducing the formation of diamond or Q-carbon based on the extent of undercooling. The thermal conductivity of as-deposited DLC and underlying substrate governs the regrowth velocity from the melt state, which in turn controls the undercooling.[11, 17]

The Raman spectrum for carbon-based materials contains peaks around 1340 cm^{-1} (*D* peak), 1560 cm^{-1} (*G* peak), and a small peak at 1140 cm^{-1} associated with strained sp^2 carbon at the interface of sp^3 clusters. A Voigt profile with peak positions fixed at 1140 cm^{-1} (*T* peak), 1340 cm^{-1} (*D* peak), and 1580 cm^{-1} (*G* peak) fits accurately to acquired Raman spectra. **Figure 1(a)** shows Raman spectra for as-deposited DLC thin films containing moderate sp^3 (48%) and Q-carbon formed after PLA processing. It was found that upon laser melt quenching, the sp^3 content increases from 48% in DLC to ~82% in Q-carbon.

The sp^3 content in as-deposited DLC films controls the thermal conductivity, degree of the undercooling and quenching rate during PLA processing. To achieve higher undercooling, DLC films with higher sp^3 content are deposited using a highly forward directed plume. **Figure 1(b)** reveals the Raman spectra of high sp^3 DLC (75%) and Q-carbon nanostructures formed after subsequent PLA processing. It is worth mentioning that due to trapping of the heat flux, undercooling is highest at the melt-substrate interface, inducing the formation of Q-carbon nanostructures. The ultrafast quenching induces interfacial instability at the melt front, resulting in observed nanostructures. Above the interface, the undercooling is lower which

results in the formation of an sp^3 deficient phase- α-carbon. A routine Voigt peak fitting was performed on Q-carbon and α-carbon to determine their sp^3 concentration, as shown in **Figure 1(c)**. The sp^3 content in Q-carbon nanostructures is determined to be 82%, whereas α-carbon has a lower sp^3 content ~60%. It is interesting to note that the most significant difference between the Raman spectra of Q-carbon and α-carbon is the *T* peak intensity. The *T* peak prominently shows up in Q-carbon spectrum, but for α-carbon it is absent. Noting that *T* peak arises from the presence of sp^3 bonded nanoclusters, its absence in α-carbon signifies that it is a graphitic phase with sp^3 defects present in it.

The microstructure of Q-carbon formed after PLA of moderate sp^3 (48%) DLC films is shown in **Figure 1(d)**. Wide gaps (4-5 μm) are noticeable between the Q-carbon filamentary nanostructures. **Figure 1(e)** reveals the microstructure of Q-carbon formed after PLA processing high sp^3 (75%) DLC thin films. The inset in **Figure 1(e)** highlights distinct α-carbon and Q-carbon phases and nanostructuring of the composite. The critical difference between Q-carbon formed from PLA of moderate sp^3, and high sp^3 thin films is the dispersion between superhard Q-carbon and α-carbon phases. Upon increasing the sp^3 content of the DLC thin films, the Q-carbon and α-carbon phases exhibit submicron dispersion, an improvement of ~7.5 times, which is needed for coating applications. As the thermal conductivity of 75% sp^3 DLC thin film is relatively higher, after PLA processing Q-carbon nanocomposites form throughout the DLC coating, as shown in **Figure 1(f)**. On termination of the PLA process, we observe the formation of a thin graphitic flake at overlayer of the nanocomposites (Raman spectra in **Figure 1(b)**) and a Q-carbon film at the substrate-film interface, as shown in **Figure 2(a)**. This phenomenon occurs due to the decrease in undercooling near the melt overlayer due to the lower amount of heat-trapped near the surface. Low regrowth velocity provides carbon atoms enough time to rearrange. Coupled with low undercooling, it results in the formation of metastable crystalline diamond or graphite phase. At a high regrowth velocity, such a rearrangement is truncated, leading to the formation of physically distinct Q-carbon and α-carbon phases. A sharp interface is noted between the α-carbon and Q-carbon phases, due to high undercooling and ultrafast quenching of the carbon melt. The transformation of homogenously deposited DLC films into physically distinct sp^3-rich

Q-carbon nanostructures and sp^2-rich α-carbon matrix elucidates laser melting and consequent ultrafast quenching.

3.2 Structure and bonding characteristics

Figure 2(a) shows a representative HAADF image of a Q-carbon nanostructure on the r-sapphire substrate. A sharp interface is noted between the Q-carbon nanostructures and sapphire, suggesting a first-order phase transformation and distinct entropy break at the interface, during the Q-carbon formation. An overlayer of α-carbon/Platinum is visible over the Q-carbon, which is a prerequisite for protecting the surface from the FIB induced damage during specimen preparation. The thickness of Q-carbon was determined to be ~30 nm, which is in good agreement with the subsequently shown estimate using finite-element Laser-Solid Interactions in Materials (SLIM) calculations. **Figure 2(b)** depicts the C-K edge EELS spectra from Q-carbon nanostructure, the parent DLC, and diamond specimens. The EEL spectrum for Q-carbon reveals two main spectral features, i.e., a sharp π^* peak (284 eV) and a broad σ^* peak (290 eV), showing the presence of both sp^2 and sp^3 hybridized atomic orbitals, respectively. By using an EELS fitting routine[18] for carbon based materials, the sp^3 content for Q-carbon in nanocomposite was determined to be 80%, which is in excellent agreement with the Raman spectroscopy results (82% sp^3). The parent DLC, consisting of sp^2 and sp^3 hybridized C atomic orbitals, shows similar characteristics in its EEL spectrum. On the other hand, pristine diamond EEL spectrum exhibits only σ^* peak due to the absence of π (sp^2) bonding. While comparing the EEL spectra of parent DLC and Q-carbon, which comprise of similar sp^2 and sp^3 composition based on Raman spectra, a distinct difference in π^* peak intensity is observed. Theoretically, it is intuitive that parent DLC (25% sp^2) should exhibit a higher π^* peak intensity as compared to Q-carbon (~20% sp^2) due to the higher sp^2 content. Surprisingly, a higher π^* peak intensity is revealed for Q-carbon as shown in **Figure 2(c)** as highlighted in the green region**.** The full-width-half-maximum (FWHM) values obtained upon Gaussian fitting for the above peaks are: 10.3 eV for Q-carbon and 7.9 eV for DLC. Also, the area under π***** peak for Q-carbon is 8.5 units, higher than that of DLC (5.3 units). This increase in π^* peak intensity is attributed to the unprecedented amount of dangling bonds in the Q-carbon nanostructures,

arising due to ultrafast quenching during the highly non-equilibrium PLA processing. It has been reported earlier that the π^* peak in carbon polymorphs is deconvoluted into $p\pi$ states arising from C sp^2 orbitals and presence of sp^2 and sp^3, uncoordinated dangling bonds leads to the generation of defect states in π^* region. [18] The influence of defect states is evident with the broadening of π^* peak and rise in its intensity in the Q-carbon. The coupling of unpaired spin magnetic moments leads to the generation of bulk ferromagnetism in the Q-carbon nanostructures. [10, 13] The ultrafast nature of melt quenching is the primary reason behind the high amount of dangling bonds present in the Q-carbon.

3.3 Mechanical properties

Figure 3(a) depicts the SPM scan of nanoindented DLC thin films highlighting uniformity of the coating. **Figure 3(b**) shows the SPM scan for Q-carbon nanocomposites, revealing that Q-carbon nanostructures (dark regions) are shallow in depth as compared to α-carbon (bright regions). It is the result of shrinkage in volume during formation of Q-carbon**.** The step shrinkage at Q-carbon nanostructures is measured to be ~40 nm consistently throughout the specimen. The Q-carbon nanostructures are embedded in the thin α-carbon matrix. In Raman spectra, SEM, and SPM imaging, stark differences are evident between the physical properties of α-carbon and Q-carbon phases.

3.3.1 Hardness

Nanoindentation is performed on the Q-carbon nanocomposites, by using a diamond indentation tip under a constant load of 1 mN. We determine the hardness of ensemble Q-carbon nanocomposites to be 67 GPa, at the Q-carbon nanostructures. The Q-carbon nanocomposites have a Young's modulus of 840 GPa. The hardness of Q-carbon nanostructures can be qualitatively ascertained by the small depth of penetration in the loading-unloading curve in **Figure 3(c)**. The hardness of as-deposited DLC is estimated to be 24 GPa with Young's modulus of 325 GPa. It shows a higher depth of penetration (35 nm) on applying 1 mN load as shown in **Figure 3(c)**. Notably, the Q-carbon nanocomposites are ~220% harder than DLC. The hardness of α-carbon phase is determined to be 18 GPa with a Young's Modulus 280 GPa. The depth of penetration

for α-carbon is determined to be 54 nm. Interestingly, upon probing the individual Q-carbon filamentary nanostructures using a sub-angstrom modulated nanoindentation technique, it revealed that Q-carbon is >40% higher hardness than diamond. [11]

Once melting occurs, and the melt front is established, it is interesting to analyze the effect of heat loss towards the surface, on the specific volume for carbon-based materials. By taking the partial derivative of pressure (*P)* in Simon equation[19], given by:

$$P = P_0 + a\left[\left(\frac{T}{T_r}\right)^c - 1\right] \quad (1)$$

where P_0 is initial pressure, T_r is the phase transformation temperature, *a* and *c* are dimensionless constants, with respect to time, we get:

$$\frac{dP}{dt} = \frac{caT^{c-1}\frac{dT}{dt}}{T_r^c} \quad (2)$$

As liquid carbon is metallic, its electronic behavior can be approximated by using the Fermi gas model. [20] The pressure associated with its internal energy (E_T) is given by:

$$P = -\frac{\partial E_T}{\partial V} = \frac{A}{V^{5/3}} \quad (3)$$

Where $A = \frac{(3\pi^2)^{2/3}\hbar^2}{5m}$ is the proportionality constant and *V* is the specific volume. So, upon differentiating equation (3) and relating the derivatives with equation (2), we get:

$$\frac{dP}{dt} = \frac{-A}{(V)^{8/3}}\frac{dV}{dt} \propto \frac{dT}{dt} \quad (4)$$

The above equation reveals that during regrowth from the melt state, the rate of change in the specific volume ($\frac{dV}{dt}$) is directly proportional to the rate of heat loss at the melt front ($\frac{dT}{dt}$). This expression explicitly shows that on increasing the rate of heat loss, the specific volume of the regrown phase, be it crystalline or amorphous, will be lower than diamond. The rate of heat loss at the melt front for the formation of Q-carbon nanocomposites, is estimated *via* SLIM calculations to be 10^{11} Ks^{-1}, which is an order higher than that of

the diamond.[10] Thus, theoretically, Q-carbon can have a higher packing fraction than diamond. The specific volume $(V) = \frac{1}{\rho} = \frac{1}{N_D * u}$, where N_D is the number density of atoms and u is the atomic mass unit for carbon. Hence, a reduction in V leads to increase in the Bulk modulus $(B) = \left(\frac{N_D}{4}\right)(98 - 10I)\rho^{1.17}$, where I is the iconicity parameter.[21] It also explains the rise in Shear modulus (G) for Q-carbon, as $G = \frac{3B(1-2\upsilon)}{2(1+\upsilon)}$, with υ as the Poisson's ratio. Further analysis for on this formalism[22] and experimental correlations for Q-carbon are presented elsewhere. [21] As the G has a direct correlation with hardness (0.151*G), this analysis opens an exciting new dimension for fabricating carbon-based nanomaterials, which are harder than diamond. [11]

3.3.2 Friction and wear coefficients in ambient conditions

An ideal coating for micro-tribology applications requires the epilayer to perform dual functions of wear resistance and lubrication. As a single material cannot provide such functionality, composites are designed for the same. A hard material anchors the film, while the matrix provides sufficient lubrication for decreasing the friction coefficient. For determining the dynamic friction and wear coefficients for Q-carbon nanocomposites, reciprocating wear tests using a pin-on-disc apparatus are performed. The amorphous Q-carbon nanocomposite coatings have an sp^3 deficient α-carbon phase, which acts as the lubricant, resulting in the reduction of friction coefficient to ~0.09 for an extended scratch length of 0.6 m as displayed in **Figure 4**. In comparison, DLC has a friction coefficient of 0.12–0.2, depending on the sp^3 content, which further worsens to 0.4 after continuous wear cycles for tests performed in ambient air conditions (relative humidity RH = 50-70%) at room temperature with load 2-5 N. [23, 24] In steady state wear regime, the volumetric loss (V) is given by:

$$V = K\frac{PL}{3H} \quad (5)$$

where H is the nanoindentation hardness, P is the applied load, L is the wear track length, and K is the dimensionless wear constant. According to this expression, to decrease wear rate, it is essential to have high

hardness and low wear constant. The dimensionless wear coefficient (*K*) is defined as the ratio of the cross-section of the wear track produced in the pin-on-disk tester to the horizontal contact area of the slider. An essential requirement for reducing the wear rate is the presence of an interfacial layer between the substrate and crystalline/amorphous coating, which serves the dual purpose of enhancing adhesion and stress-relief. The superhard Q-carbon nanostructures anchor the lubricating α-carbon matrix with an additional flat underlayer of Q-carbon, which performs the stress-relief.[25] As this interfacial layer of Q-carbon forms by ultrafast quenching of the super undercooled carbon melt, it has excellent adhesion with the substrate and results in *K* value of $1x10^{-6}$ against the diamond conical tip. Upon melting of carbon, the metallic melt settles uniformly on the sapphire substrate. It is the reason for the extreme flatness of Q-carbon formed due to ultrafast melt quenching and high undercooling. It is noteworthy to mention that usage of sapphire and steel balls for wear testing resulted in extensive wear of the balls. For high sp^3 DLC, the wear coefficient was determined to be $K \sim 9x10^{-6}$ which is consistent with previously reported data. [26, 27] The reason for higher wear rate in DLC is shearing at the asperity contacts. Due to shearing, large chunks come out of the film creating debris, which increase the friction coefficient for the coating with time. [28, 29] Due to the nanostructuring of the Q-carbon composites, minimal chunks are produced by the shearing force of the scratch tip creating superhard and ultrafine debris. The probe secludes the debris as it traverses the film for long cycles, preventing a rise in frictional force. This phenomenon is revealed in **Figure 4** with the friction coefficient of Q-carbon nanocomposites remaining constant for the long scratch length of 0.6 m.

Veprek et al. proposed a model of superhard nanocrystalline grains embedded in an amorphous matrix, which separated them by 1-3 nm to achieve dislocation suppression and hinder crack propagation. [30] On subsequent laser annealing, Q-carbon leads to nanodiamond nucleation, which will further anchor the coating against wear rate. [10] For large microdiamond films, diamond on diamond abrasion will occur, and friction coefficient will increase due to the strong C-C bonding at the interface. [27, 31] Wear in diamond drill bits occurs *via* fatigue mechanism, where formation and growth of cracks lead to fracture of

the diamond. [32] As Q-carbon nanocomposites are amorphous, they deter crack propagation and fatigue failure, therefore becoming a much better choice for wear resistant coatings.

3.4 Heat conduction and laser melting in disordered solids

In solids, heat conduction (K_T) occurs *via* electrons (K_e) and phonons (K_P), i.e., $K_T = K_P + K_e$. In covalently bonded bulk carbon materials, heat conduction mainly occurs *via* acoustic phonons. For ordered crystalline bulk carbon polymorphs like graphite (*a-axis*), at higher temperatures K_P decreases as T^{-a}; where *a* is 0.51 for *c-axis* K_e in graphite.[33] For disordered solids like DLC, electron hopping is localized due to unavailability of π-π conjugated bonds as the sp^2 bonding is truncated by sp^3 hybridized states. [34] Here, K_P rises monotonically at low temperatures and achieves a constant value at higher temperatures ~300-500 K. [35] Also, for DLC K_P scales linearly with the sp^3 content. [36] Interestingly, amorphous films which are highly graphitic have K_P ~ 0.3 W m^{-1} K^{-1} and the tetrahedrally bonded high sp^3 DLC thin films can have K_P as high as 10 W m^{-1} K^{-1}. [36] PLA causes localized melting of the thin film in the super undercooled state above threshold energy density. It results in the formation of a homogenous melt around 4000 K. This phenomenon occurs as at high temperatures due to the entropy overriding the enthalpy contribution in Gibbs free energy. Experimental studies have revealed that the melt is metallic and its properties can be approximated *via* classical free electron gas model. [20, 37] Once melting occurs, the resulting properties and structural evolution of the solid are dependent on regrowth velocity of the solid from melt state. After performing PLA, the solidification terminates in less than 200 ns making this an ultrafast quenching process. The quenching rate is thermodynamically driven by the substrate and thin film thermal conductivity. [38] On decreasing the substrate thermal conductivity, it traps heat leading to an increase in temperature at the interface. Further, an increase in the sp^3 content of the DLC thin film results in enhancement of bulk thermal conductivity at the regrown solid-liquid interface, causing high thermal losses at the surface. Therefore, the DLC sp^3 content induces a rise in regrowth velocity at the melt interface.

The net rate of atomic jumping for interfacial regrowth at a liquid-solid interface for non-equilibrium processing at the temperature (*T*) is given by:

$$V \sim \frac{D_\alpha f}{\lambda f_D}\left(1 - exp\left(-\frac{\Delta G}{k_B T}\right)\right) \quad (6)$$

Here, D_α is diffusivity in melt near the interface ~10^{-8} m^2s^{-1}, f_D is the geometric factor associated with diffusion, which is unity for isotropic amorphous melt and solid state, *f* is the fraction of available sites for the exchange of C atoms and λ is the atomic jump distance across the melt interface. In this formalism, equality of interfacial number density of atoms in liquid and solid phases is assumed. [39] On reaching equilibrium condition, ΔG approaches zero and regrowth ceases to exist. However, at the substrate/melt interface, undercooling is high enough to trigger formation of metastable Q-carbon nanostructures. [10] Near equilibrium, $\Delta G \sim 0$ and this equation simplifies to:

$$V(T) = \frac{V(T_m) L_m \Delta T_u}{R T_m^2} \quad (7)$$

where $V(T_m)$ is the kinetic pre-factor, L_m is the latent heat of melting, ΔT_u is the undercooling. The equation reveals that regrowth velocity V(T) increases with rise in undercooling ΔT. An increase in regrowth velocity arrests energetically driven phase segregation of sp^2 and sp^3 atoms. It results in the formation of amorphous Q-carbon due to the rise in interfacial instability above critical undercooling (ΔT_u^c)

$$\Delta T_u^c > T_m^{dia} - T_m^\alpha \quad (8)$$

where T_m^{dia} and T_m^α are the melting points for diamond and amorphous carbon, respectively. Due to the difference between the Gibbs free energy for disordered amorphous carbon and crystalline diamond, it is thermodynamically possible to attain amorphous regrowth at the melt interface, above critical undercooling (ΔT_u^c). [38, 40]

3.5 Finite element SLIM modeling

Finite-element SLIM programming [41, 42] is performed to analyze the complex laser-solid interaction simulations for understanding the structural transformation of DLC into Q-carbon nanocomposites. As the laser beam dimensions are significantly larger than melt depth (~50-100 nm), column approximation is utilized to simulate the laser-solid interactions using 1-D finite element method. The approximation is

viable as the heat flow perpendicular to the film has an order higher magnitude in comparison with the film surface, causing it to collapse as a 1-D heat flow problem. The laser parameters- λ=193 nm, FWHM = 20 ns and corresponding reflectivity for solid DLC, and the carbon melt are used as input parameters simulate the PLA. The surface temperature-time plots in **Figure 5(a)** reveals that 0.4 J cm^{-2} is the critical energy density to induce surface melting. At the onset of melting, the melt gets heated up with maxima ~18 ns, as shown in the inset of **Figure 5(a)**. On increasing the laser pulse energy density, this heating gets further enhanced leading to high temperatures ~4600 K for 1 J cm^{-2} nanosecond PLA. The liquid carbon is metallic and possesses a thermal conductivity of 290 W m^{-1} K^{-1} [43], so it cools down rapidly to melting temperature as the pulse terminates. The maxima melt profiles at respective energy densities are highlighted in **Figure 5(b)**. The figure reveals that melt depth increases monotonically with laser pulse energy density. The increase in regrowth velocity translates into a rise in the interfacial instability and decrease in the cellular wavelength of the Q-carbon cell structures.[39] The decrease in cell wavelength enhances dispersion of superhard Q-carbon and soft α-carbon phases throughout the coating, inducing a large-area coverage of nanocomposites on the substrate.

4. Conclusions

We have created Q-carbon nanocomposites by nanosecond laser melting of amorphous carbon thin films with high sp^3 content. The Q-carbon nanocomposites form due to ultrafast quenching of the super undercooled melt state of carbon. The two phases of nanocomposites – sp^3-rich Q-carbon and sp^2 rich α-carbon have distinct physical and mechanical properties. Due to increased undercooling, the nanocomposites exhibit ~7.5 times higher dispersion between the Q-carbon and α-carbon phases, as compared to Q-carbon grown by PLA of DLC with moderate sp^3 content. This enhanced dispersion at the nanoscale makes the Q-carbon composites a viable candidate for coating applications. The Q-carbon nanocomposites have a hardness of 67 GPa, showing an improvement of 220% over parent DLC. The α-carbon phase is soft with a hardness of 18 GPa. This structure is critical in providing the coating with lubrication reducing friction coefficient to 0.09 and wear coefficient to $1x10^{-6}$. The nanocomposites show

improved performance because they contain nanostructured superhard Q-carbon and soft lubricating α-carbon phases which form an adherent coating on the substrate. The fine details in core-loss EEL spectra; revealed an increment in the π^* peak intensity for Q-carbon nanostructures, in comparison with parent DLC. This rise in π^* peak intensity is a result of the increase in the number of dangling bonds formed during to the ultrafast quenching from the molten carbon state. The magnitude of ultrafast quenching and the mechanical properties observed in the Q-carbon nanocomposites are correlated with the structure and bonding characteristics using Raman spectroscopy, core-loss EEL spectroscopy, nanoindentation and wear measurements, in addition to the theoretical SLIM calculations. These studies show that Q-carbon nanocomposites have improved hardness, lower friction and wear coefficients and higher C packing fraction as compared to as-deposited DLC coatings. We envisage that this discovery of superhard Q-carbon nanocomposites will result in furthering the research on carbon-based materials for coating applications.

Supplementary material

See supplementary material for calibration of nanoindentation experiments, performed on fused Quartz and r-sapphire substrates.

Acknowledgments

We are grateful to Fan Family Foundation Distinguished Chair Endowment for Prof. J. Narayan. Ritesh Sachan acknowledges the National Academy of Sciences (NAS), USA for awarding the NRC research fellowship. This research work was performed under the National Science Foundation (Award Number DMR- 1560838, DMR- 1735695). Part of the analysis was conducted at the Analytical Instrumentation Facility (AIF) at North Carolina State University, supported by the state of North Carolina. We are also pleased to acknowledge technical help and discussions with John Prater, Sudhakar Nori, Punam Pant, Adele Moatti, Ariful Haque, Alexander Niebroski, William Stradder, Chuck Mooney, Roberto Garcia and Fred Stevie.

References

[1] Chen X and Narayan J 1993 *J. Appl. Phys.* 74 4168-73

[2] Wei Q and Narayan J 2000 *Int. Mat. Rev.* 45 133-64

[3] Gille G and Rau B *Thin Solid Films* 120 109-21

[4] Jarratt M, Stallard J, Renevier N and Teer D 2003 *Diam. Relat. Mater.* 12 1003-7

[5] Fryda M, Taube K and Klages C P 1990 *Vacuum* 41 1291-3

[6] Bewilogua K, Cooper C V, Specht C, Schröder J, Wittorf R and Grischke M 2000 *Surf. Coat. Technol.* 132 275-83

[7] Wang D-Y, Chang C-L and Ho W-Y 1999 *Surf. Coat. Technol.* 120 138-44

[8] Montross C S, Wei T, Ye L, Clark G and Mai Y-W 2002 *Int. J. Fatigue* 24 1021-36

[9] Narayan J, Godbole V and White C 1991 *Science* 252 416-8

[10] Narayan J and Bhaumik A 2015 *J. Appl. Phys.* 118 215303

[11] Narayan J, Gupta S, Bhaumik A, Sachan R, Cellini F and Reido E 2018 *MRS Comm.* 1-8

[12] Gupta S, Sachan R, Bhaumik, Pant P and Narayan 2018 *MRS Comm.* J 1-8

[13] Bhaumik A, Nori S, Sachan R, Gupta S, Kumar D, Majumdar A K and Narayan J 2018 *ACS Appl. Nano Mater.* 1 807–19

[14] Narayan J, Bhaumik A, Gupta S, Haque A and Sachan R 2018 *Mater. Res. Lett.* 6 353-64

[15] Bhaumik A, Sachan R and Narayan J 2017 *ACS Nano* 11 5351-7

[16] Bhaumik A, Sachan R, Gupta S and Narayan J 2017 *ACS Nano* 11 11915-22

[17] Gupta S, Bhaumik A, Sachan R and Narayan J 2018 *JOM* 70 450-55

[18] Bruley J, Williams D B, Cuomo J and Pappas D 1995 *J. Microsc.* 180 22-32

[19] Babb Jr S E 1963 *Rev. Mod. Phys.* 35 400

[20] Steinbeck J, Dresselhaus G and Dresselhaus M 1990 *Int. J. Thermophys.* 11 789-96

[21] Liu A Y and Cohen M L 1990 *Phys. Rev. B*, 41 10727.

[22] Gao F 2006 *Phys. Rev. B* 73 132104

[23] Grill A 1997 *Surf. Coat. Technol.* 94 507-13

[24] Grill A 1999 *Diam. Relat. Mater.* 8 428-34

[25] Voevodin A, Walck S and Zabinski J 1997 *Wear* 203 516-27

[26] Agarwal A, Shih C, Harper M, Bauer C and Bhushan B 1989 Tribology and mechanics of magnetic storage devices Springer Science & Business Media

[27] Grill A and Patel V 1993 *Diam. Relat. Mater.* 2 597-605

[28] Denape J and Lamon J 1990 *J. Mater. Sci.* 25 3592-604

[29] Sawyer W G, Freudenberg K D, Bhimaraj P and Schadler L S 2003 *Wear* 254 573-80

[30] Vepřek S and Reiprich S 1995 *Thin Solid Films* 268 64-71

[31] Grill A 1993 *Wear* 168 143-53

[32] Memming R, Tolle H and Wierenga P 1986 *Thin Solid Films* 143 31-41

[33] Steinbeck J, Braunstein G, Dresselhaus M, Venkatesan T and Jacobson D 1985 *J. Appl. Phys.* 58 4374-82

[34] Cahill D G and Pohl R 1989 *Solid State Commun.* 70 927-30

[35] Balandin A A 2011 *Nat. Mater.* 10 569-81

[36] Shamsa M, Liu W, Balandin A, Casiraghi C, Milne W and Ferrari A 2006 *Appl. Phys. Lett.* 89 161921

[37] Heremans J, Olk C, Eesley G, Steinbeck J and Dresselhaus G 1988 *Phys. Rev. Lett.* 60 452

[38] Cullis A, Webber H, Chew N, Poate J and Baeri P 1982 *Phys. Rev. Lett.* 49 219

[39] Narayan J 1982 *J. Appl. Phys.* 53 8607-14.

[40] Spaepen F, Turnbull D, Ferris S, Leamy H and Poate J 1979 Laser-Solid Interactions and Laser Processing (vol 50)

[41] Singh R K and Narayan J 1989 *Mater. Sci. Engg.: B* 3 217-30

[42] Singh R K and Narayan J 1990 *Phys. Rev. B* 41 8843

[43] Neto A C, Guinea F, Peres N M, Novoselov K S and Geim A K 2009 *Rev. Mod. Phys.* 81 109

Figures

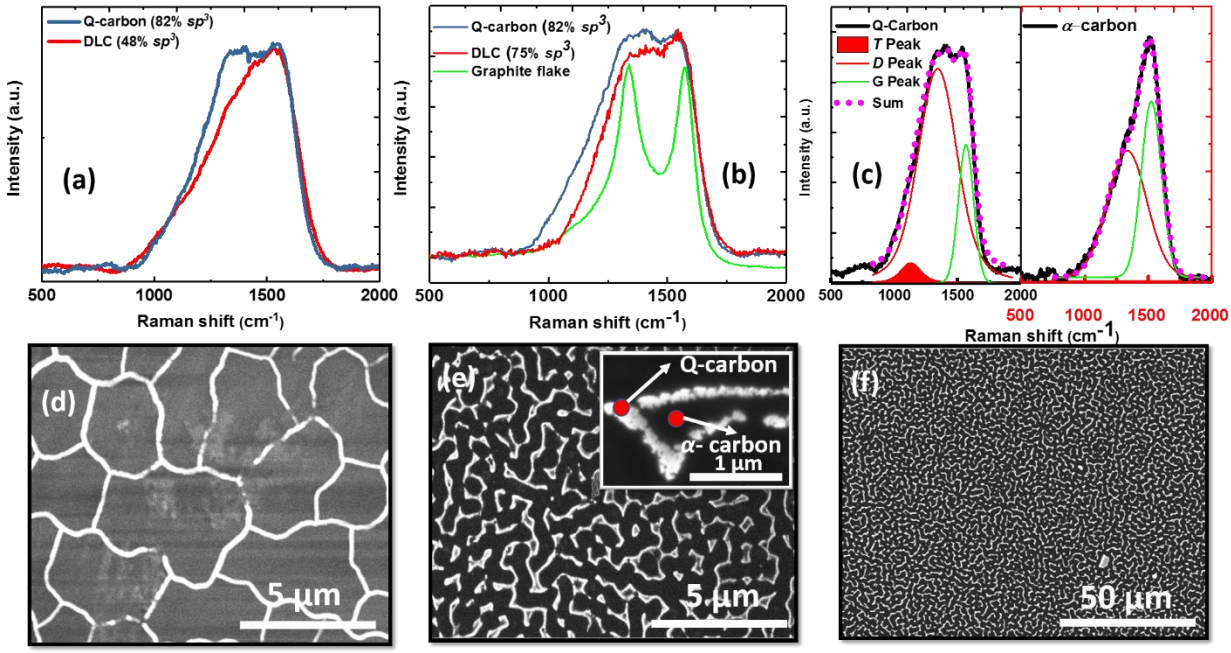

Figure 1. Raman spectra for (a) as-deposited DLC (48% sp^3) and Q-carbon; (b) as-deposited DLC (75% sp^3), Q-carbon and graphitic flake formed over Q-carbon nanocomposites; (c) Voigt peak fitting for Q-carbon and α-carbon phases of Q-carbon nanocomposites formed after PLA processing; FESEM imaging for (d) microstructure of Q-carbon formed from PLA moderate sp^3 (48%) DLC; (e) illustrates the 7.5 times increased dispersion of Q-carbon and α-carbon phases in the Q-carbon nanocomposites formed from PLA high sp^3 (75%) DLC; the inset in (e) shows a single Q-carbon cell inside α-carbon matrix; (f) highlights the large-area coverage of Q-carbon nanocomposites.

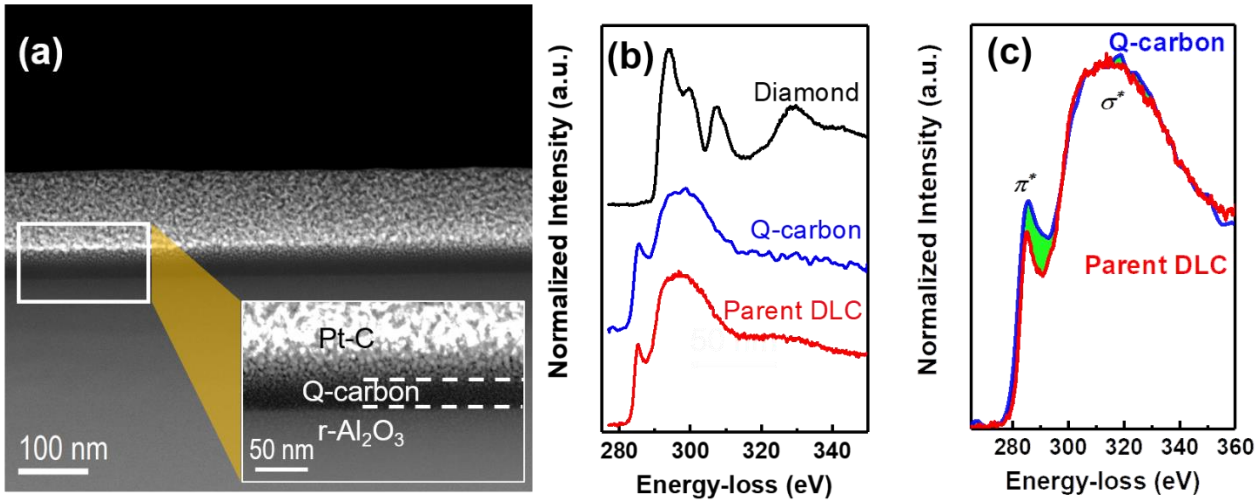

Figure. 2. (a) High-angle-annular Dark Field image for Q-carbon nanocomposites on r-sapphire revealing an amorphous, sharp, continuous ~30 nm thick Q-carbon nanostructure in the magnified inset; (b) The contrasting core-loss EEL spectra for Q-carbon, Diamond and 75% sp^3 as-deposited DLC; and (c) The fine details in π^* peaks for Q-carbon and DLC indicate a rise in π^* peak intensity, inherent asymmetry and peak broadening (green region) in π^* peak for Q-carbon.

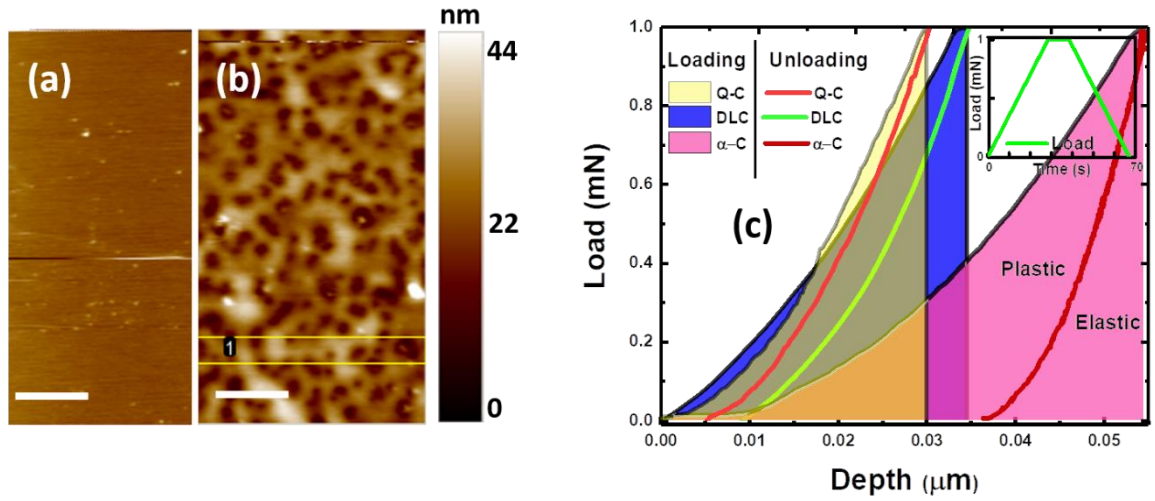

Figure 3. SPM scans showing the morphology of (a) as-deposited DLC; (b) Q-carbon nanocomposites; The scale bar in (a) and (b) is 2 μm. (c) Loading and unloading curves for Q-carbon nanocomposites (Q-C) (yellow) with a hardness of 67 GPa, and high sp^3 DLC exhibiting a hardness of 24 GPa (blue) and α-carbon with a hardness of 18 GPa (pink).

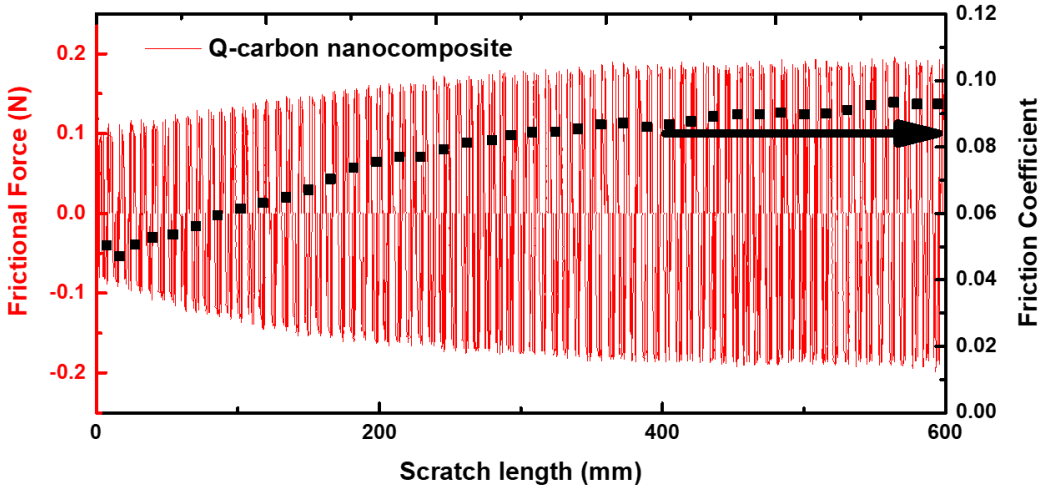

Figure 4. Reciprocating wear testing profile for Q-carbon nanocomposites with a friction coefficient of 0.09 maintained in a long scratch length of 600 mm.

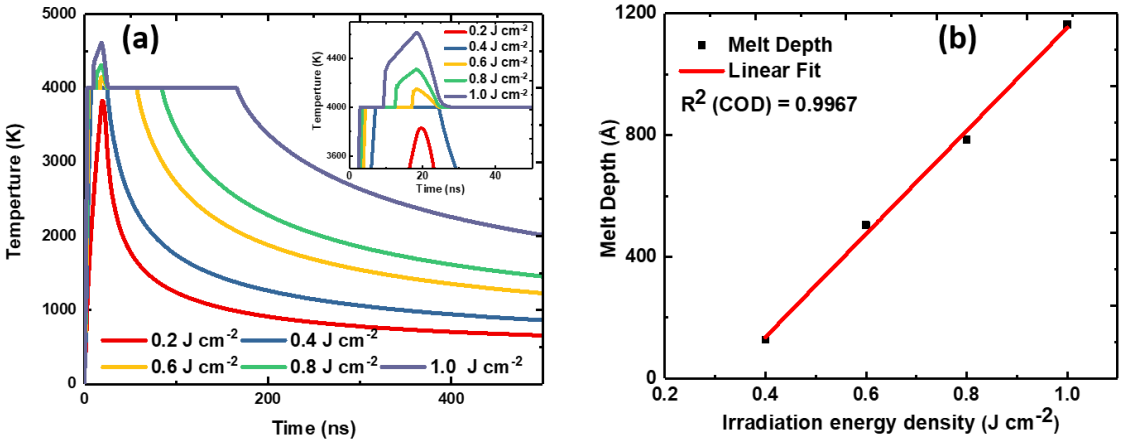

Figure 5. (a) Simulated SLIM PLA thermal profiles for high sp^3 (75%) DLC thin films. The inset shows magnified profiles at the onset of melting, and (b) Maxima in melt depth as a function of laser annealing energy density for DLC with 75% sp^3 content for various PLA energy densities.